Applied Thermal Engineering 235 (2023) 121327

Contents lists available at ScienceDirect

Applied Thermal Engineering

journal homepage: www.elsevier.com/locate/apthermeng

Research Paper

Experimental and computational investigation of thermal performance and fluid flow in two-phase closed thermosyphon

Sehyeon Cho [a], Daeyoung Kong [a], Gyohoon Geum [a], Sukkyung Kang [b], Jin Hyeuk Seo [b], Jun Soo Kim [c], Seong Hyuk Lee [c], Jungho Lee [b,*], Hyoungsoon Lee [a,c,*]

[a] Department of Intelligent Energy and Industry, Chung-Ang University, Seoul 06974, South Korea
[b] Department of Mechanical Engineering, Ajou University, Suwon 16499, Republic of Korea
[c] School of Mechanical Engineering, Chung-Ang University, Seoul 06974, South Korea

ARTICLE INFO

Keywords:
Waste heat recovery
Two-phase closed thermosyphon
OpenFOAM
Boiling
Condensation

ABSTRACT

Over the last two decades, energy recovery has become increasingly important in the transition from fossil fuels to green energy. Waste heat recovery, such as the two-phase closed thermosyphon (TPCT) type of heat exchanger, is a highly efficient energy recovery technique. However, accurately predicting the thermal performance and flow patterns in TPCTs is challenging due to the complex physics of phase-change phenomena. A new predictive model is suggested that can provide improved accuracy when predicting thermal performance and flow patterns in TPCTs. An experimental study was conducted to acquire the data, and the results were compared with computational results obtained from the new proposed model. The model uses the volume of fluid (VOF) model with the Lee model for the phase change process in OpenFOAM v2106. To increase accuracy, the saturation temperature and vapor density were defined as a function based on the mass balance in the TPCT. In addition, a simulation was conducted to predict the thermal performance and flow patterns in a TPCT, during which the effects of the empirical value of the mass transfer intensity factor were investigated. The study is expected to provide insights into phase-change modeling with high accuracy and an understanding of the thermal characteristics of TPCTs.

1. Introduction

Significant carbon dioxide emissions from using excessive fossil fuels have resulted in environmental pollution and global warming. Accordingly, a transition from fossil fuels to green energy is crucial for minimizing carbon emissions. Among the various green energy plans for sustainable development, energy recovery technology has attracted great interest over the last two decades due to its advantage of reserving additional energy from existing facilities [1]. Waste heat recovery [2] is one of the most promising methods in energy recovery technology (using technology such as thermoelectric [3] and piezoelectric devices [4]), owing to its exceptional energy recovery performance and wide application range—from residential facilities to power plants. Predominantly, waste heat recovery is achieved through energy recovery heat exchangers, including shell-and-tube and double-pipe type heat exchangers. Of these, shell-and-tube type heat exchangers are the most preferred due to their high efficiency and reliability. Over the past four decades, many studies have enhanced the heat recovery rates and efficiency of shell-and-tube heat exchangers, by using technologies such as finned tubes, baffles, and nanofluids [5–7]. In addition, many effectively designed shell-and-tube heat exchangers have recently adopted two-phase closed thermosyphon (TPCT) tubes instead of conventional tubes, due to their noticeably higher heat transfer efficiency [8].

TPCTs are in the spotlight as a passive heat transfer device because no driving power is required, as they work using gravitational force. A TPCT consists of three sections: the evaporator section at the bottom, the adiabatic section in the middle, and the condenser section at the top. In a TPCT, heat is applied to the evaporator section and evaporates (or boils) the working fluid. The boiled working fluid in the evaporator section then rises and moves to the condenser section with the aid of gravitational force. Then, the vapor is condensed into a liquid on the condenser wall by releasing heat. Finally, the condensed liquid falls back into the evaporator section, again due to gravitational force. With the aid of boiling and condensation heat transfer, TPCTs exhibit superior heat transfer performance compared to conventional tubes. Therefore, they have been widely used for waste heat recovery and in various other fields, such as solar cells [9], permafrost applications [10], and the

* Corresponding authors.
E-mail addresses: jungholee@ajou.ac.kr (J. Lee), leeh@cau.ac.kr (H. Lee).

https://doi.org/10.1016/j.applthermaleng.2023.121327
Received 16 February 2023; Received in revised form 2 August 2023; Accepted 10 August 2023
Available online 15 August 2023
1359-4311/

Nomenclature

C_p	specific heat at constant pressure
C_v	specific heat at constant volume
d	diameter
FR	filling ratio
g	acceleration due to gravity
h	enthalpy
h_{fg}	latent heat
I	current
k	thermal conductivity
k_{eff}	effective thermal conductivity
L	length
m	mass
n	normal
P	pressure
Q	heat transfer rate
q''	heat flux
R_{th}	total thermal resistance
r	mass transfer intensity factor
S	source
T	temperature
T_{sat}	saturation temperature
TPCT	two-phase closed thermosyphon
t	time
u	velocity
u_r	compression velocity
v	volume
V	voltage

Greek symbols

α	volume fraction
κ	curvature
μ	dynamic viscosity
ν	kinetic viscosity
ρ	density
σ	surface tension

Subscripts

avg	average
c	condensation
e	evaporation
f	fluid
g	gas
in	inlet
out	outlet
w	wall

Superscripts

i	iteration
i-1	previous iteration

thermal management of power electronics [11,12] and data centers. Many types of research have been conducted to improve the thermal performance of TPCTs by adjusting various performance parameters, such as the filling ratio (FR), surface coating, and working fluid [13–15]. Most of these TPCT studies have adopted experimental investigations, due to the poor computational accuracy of complex phase-change phenomena. Recently, researchers have developed various phase-change techniques to improve the accuracy of TPCT simulations [16–22]. Alizadehdakhel *et al.* [16] conducted the first computational attempt at studying a two-dimensional TPCT simulation using the volume of the fluid (VOF) model and analyzed the effects of heat flux and FR on temperature distribution and thermal performance. Similarly, Jubori and Jawad [17] studied the effect of various operating conditions (such as inclination angle, FR, and heat flux) on thermal performance. Several studies have also been conducted on how the geometrical effect can affect the performance of TPCTs. Tarokh *et al.* [18] investigated the thermal performance of TPCTs with a vortex generator inside the TPCT geometry. Similarly, Fertahi [19] installed external fins on the condenser wall to enhance heat transfer and implemented a computational investigation. Yuan *et al.* [20] focused on the effect of non-condensable gas in TPCTs, while Jafari *et al.* [21] investigated unsteady computational analyses. In addition, one study investigated specific flow patterns, such as geyser boiling [22]. Dhanalakota *et al.* [23] investigated the effect of several variables on flat-shaped TPCTs, including the FR, working fluid, and heat sources.

Most relevant previous studies on TPCTs have adopted Lee's phase change model [24] due to its mathematical simplicity and ease of implementation with commercial CFD software (including ANSYS Fluent). When using the Lee model to simulate phases changes, the most important aspect is to determine two key parameters: i) the mass transfer intensity factor r [s^{-1}], and ii) the saturation temperature T_{sat} [K]. The mass transfer intensity factor is a constant that is used directly to calculate the mass transfer rate of evaporation or condensation. In many relevant previous studies, an arbitrary value was selected for the mass transfer intensity factor from within the following value and ranges: $r_e = 0.1$ s^{-1} and $r_c = 0.1$–1000 s^{-1} [16,18,22]. In contrast, several studies empirically calibrated the values based on experimental data [25–29]. For example, Wang *et al.* [26] employed 0.02–2 s^{-1} for evaporation and 100–10,000 s^{-1} for condensation, while Kafeel *et al.* [27] used 0.1 s^{-1} for evaporation and a value updated in each iteration (such as $r_{c,old} - r_{e,old}$ $[(m_c\text{-}m_e)/\max(m_e, m_c)]$) for condensation. Xu *et al.* [30] also used a value updated in each iteration: $r_{e,old} - r_{e,old}$ $[(m_e\text{-}m_c)/\max(m_e, m_c)]$ for evaporation and $r_{c,old} - r_{c,old}$ $[(m_c\text{-}m_e)/\max(m_e, m_c)]$ for condensation. Kim *et al.* [31] considered the density ratio between the liquid and vapor for the mass transfer intensity factor to make the balance of mass transfer in a single cell, then employed $r_e = 0.1$ s^{-1} for evaporation and $r_e \times (\rho_f / \rho_g)$ for condensation. Tarokh *et al.* [18] also considered the same density ratio as Kim *et al.* [31]. Relevant previous computational studies are summarized in Table 1. For the saturation temperature, many previous studies used 373 K for water based on the assumption of saturation temperature at ambient pressure [17,19,31–33] because it is difficult to measure in practical applications. However, most TPCTs that use water are operated under a vacuum to attain low wall temperatures and as a result of the elimination process of non-condensable gas from the working fluid. Moreover, the inner pressure increases according to the applied heat flux in the evaporator section, meaning T_{sat} would differ from 373 K under atmospheric pressure during operation. Unfortunately, an inaccurate value of T_{sat} yields mispredictions of evaporation and condensation rates, resulting in poor prediction accuracy when determining the thermal performance of a TPCT. When the working fluid undergoes a phase change, its temperature is fixed in T_{sat} due to the use of latent heat. The use of constant T_{sat} results in a constant wall temperature, irrespective of changes in operating conditions (such as heat flux or operating pressure). However, we anticipate that it would be possible to predict TPCT performance with high accuracy in simulations by implementing the functional T_{sat} which T_{sat} works based on the mass balance as proposed in this study. The functional T_{sat} would increase or decrease corresponding to the operating conditions, while the constant T_{sat} could not increase or decrease.

The present study provides both experimental and computational for determining the thermal performance of TPCTs. The thermal performance was experimentally determined in various TPCT operating

Table 1
Current status of computational research on TPCTs.

Author(s)	Geometry (D × L) [mm^2]	Inclination []	Working fluid	Filling ratio	r_e [s^{-1}]	r_c [s^{-1}]	Saturation Temperature [K]	Note
Alizadehdakhel *et al.* (2010)	19 × 1000	90	Water	0.3 – 0.8	0.1	0.1	350	–
Fadhl *et al.* (2013)	22 × 500	90	Water	0.5	0.1	0.1	373	–
Kafeel & Khurram (2014)	39 × 980	90	Water	0.3	0.1	Eq. (c)	350	Pulsed heat flux condition
Fadhl *et al.* (2015)	22 × 500	90	R134a, R404a	0.5	0.1	0.1	Not specified	–
Kim *et al.* (2015)	22 × 500	90	Water	0.5	0.1	$r_{evap}\times(\rho_f/\rho_g)$	373	density ratio to adopt mass transfer intensity factor
Alammar *et al.* (2016)	22 × 400	10 – 90	Water	0.25 – 1	0.1	0.1	373	–
Jafari *et al.* (2017)	35 × 500	90	Water	0.16 – 1.35	Fine tuned	0.16 – 1.35	Not specified	Unsteady thermal characteristics
Fertahi *et al.* (2018)	9.8 × 190	90	water	0.25	Fine tuned	0.25	373	Externally finned geometry
Wang *et al.* (2018)	18 × 440	90	Water	0.75	Fine tuned	Same with r_{evap}	318	Numerical modeling of geyser boiling in TPCT
Xu *et al.* (2018)	25.4 × 240	15 – 90	water	0.25	Eq. (a)	Eq. (c)	Not specified	Contact angle modeling
Wang *et al.* (2019)	38 × 2000	90	Ammonia	0.2 – 0.3	0.02 – 2	$100\times r_{evap}$ – $10000\times r_{evap}$	Not specified	Different heating length
Hosseinzadeh *et al.* (2020)	22 × 500	90	Water, 1-butanol-water	0.5	0.1	0.1	Not specified	–
Yao *et al.* (2020)	21 × 600	90	Water	0.5	Fine tuned	Eq. (d)	322	
Jobori and Jawad (2020)	22 × 400	15 – 90	Water	0.25 – 0.9	Eq. (b)	Eq. (e)	373	–
Yuan *et al.* (2020)	9.52 × 1250	90	R134a	0.8	0.1	0.1	As Experimental data	effect of non-condensable gas
Tarokh *et al.* (2021)	22 × 500	90	Water	0.5	0.1	$r_e\times(\rho_f/\rho_g)$	373	Vortex generation geometry
Xiao *et al.* (2022)	47 × 1000	90	CuO-H_2O	0.15 – 0.25	Fine tuned	0.15 – 0.25	Not specified	–
Present Study	17 × 400	90	Water	0.75	0.025 – 0.075	5×10^4 – 100×10^4	Eq. (f)	–

r_e: Eq. (a) $r_{e,old} - r_{e,old}\left\{\frac{m_e - m_c}{\max(m_e,\ m_c)}\right\}$, Eq. (b) $\frac{6\rho_g\Delta h\sqrt{M}}{D_{sm}(\rho_f-\rho_g)\sqrt{2\pi RT_{sat}}}$,

r_c: Eq. (c) $r_{c,old} - r_{c,old}\left\{\frac{m_c - m_e}{\max(m_e,\ m_c)}\right\}$, Eq. (d) $\frac{dr_c}{dt} = 0.001$ (if P > P_{sat}), Eq. (e)$\frac{6\rho_f\Delta h\sqrt{M}}{D_{sm}(\rho_f-\rho_g)\sqrt{2\pi RT_{sat}}}$.

T_{sat}: Eq. (f)$386.74\times\rho_g^{0.058} - 10$.

※The Lee model was adopted as a phase change model for all paper.

$S_g = r_c\alpha_g\rho_g\frac{(T-T_{sat})}{T_{sat}}$ for condensation $(T<T_{sat})$, $S_f = r_e\alpha_f\rho_f\frac{(T-T_{sat})}{T_{sat}}$ for evaporation $(T>T_{sat})$.

conditions through precise thermal measurements, and we analyzed the thermal performance trend in detail. Then, the experimental results were used to map a detailed simulation technique for the phase change process in TPCTs. A facile method for estimating the saturation temperature was adopted to accurately predict the saturation temperature in TPCTs, with a significantly improved convergence rate during phase change simulations. This is based on mass balance, which is the most accurate method for closed systems because the mass is not allowed to be created or removed. The predictions using our method exhibited excellent accuracy with a maximum difference of temperature on the wall of TPCT within ±3 K. Moreover, the effect of mass transfer intensity factor on the thermal characteristics in TPCTs was extensively investigated. Ultimately, this study provides useful insights into the choice of empirical constants and saturation temperatures when simulating phase changes in TPCTs.

2. Experimental method

2.1. TPCT fabrication and experimental setup

The thermosyphon was fabricated from copper, with an inner diameter of 17 mm, a thickness of 1 mm, and a length of 400 mm. It comprised two sections (an evaporator and a condenser) of lengths 250 and 150 mm, respectively. As water has the highest figure of merit (FOM), which is a performance indicator for working fluids in TPCTs, this was used as the working fluid. To fabricate the TPCT, the air inside was removed using a vacuum pump and the final vacuum level reached below 10^{-3} mTorr. Next, distilled water was boiled at atmospheric pressure for 2 h to remove any non-condensable gas (NCG) dissolved in the working fluid, which would significantly increase the thermal resistance of a TPCT. Subsequently, the TPCT was manufactured by injecting degassing water into the tube under a vacuum. The FR is defined as the volume of the working fluid to the volume of the evaporator, which was controlled through an injection chamber with a volume equal to the injection amount.

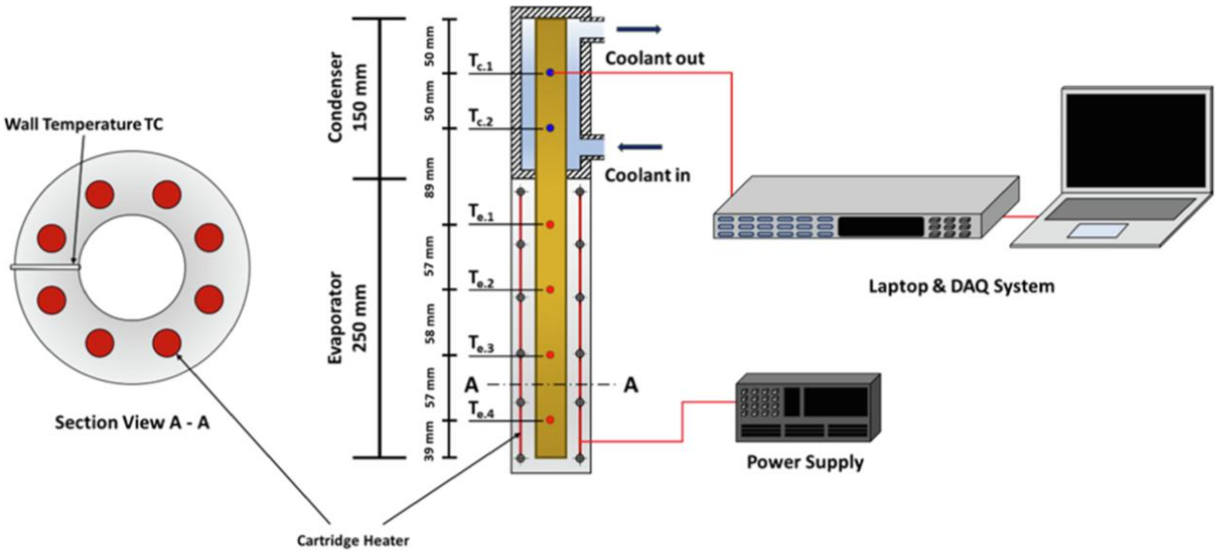

Fig. 1. Schematic configuration of experimental setup.

The entire experimental setup for determining the thermal performance of the TPCT is displayed in Fig. 1. In the evaporator section, the heat was supplied by cartridge heaters using a DC power supply (Keysight N8741A). A total of eight cartridge heaters were inserted uniformly to supply heat under constant heat flux conditions. The heat was dissipated from a condenser section surrounded by a water jacket connected to an external circulation chiller. The evaporator and condenser sections were insulated using glass wool to prevent any heat loss during the experiment. T-type thermocouples with a diameter of 1/16″ were installed in each evaporator and condenser section to measure the wall temperature of the TPCT. The measured data were acquired using a VTI Instruments EX 1032A data acquisition system. Various operating ranges of heat flux (4–30 kW/m^2) and FR (5%–75%) were tested to investigate their effect on thermal performance in TPCTs.

2.2. Data reduction

The analysis of the thermal performance of a TPCT involved a comparison of the total thermal resistance R_{th} [K/W] obtained from the following equation:

$$R_{th} = \frac{T_{w,e} - T_{w,c}}{q''} \tag{1}$$

where $T_{w,e}$ and $T_{w,c}$ are the wall temperatures of the evaporator section and condenser section, respectively. The wall temperature was obtained by averaging the measured temperatures for 300 s when steady-state was reached. The heat flux (q'' [W/m^2]) was calculated from the voltage and current generated by the DC power supply.

The uncertainty analysis was conducted using the "Guide to the Expression of Uncertainty in Measurement by International Organization for Standardization (ISO GUM)" [34].

$$\delta R_{th} = \sqrt{\sum_{i=1}^{n}\left(\frac{\partial R_{th}}{\partial x_i}\delta x_i\right)^2} \tag{2}$$

The experimental uncertainties of the primary measurement variables were as follows: 0.1% for voltage, 0.2% for current, and 0.5 °C for temperature. From Eq. (2), the relative expanded uncertainty for overall thermal resistance was between 1.5% and 9.4%.

3. Computational method

3.1. Governing equations

The volume-of-fluid (VOF) method [35] was employed in the commercial open-source package OpenFOAM v2106 to simulate the phase change mass transfers in the TPCT. The governing equations (including the volume fraction equation) are listed below.

Volume fraction equation:

$$\frac{\partial \alpha_f}{\partial t} + \nabla\cdot(\alpha_f u) + \nabla\cdot(\alpha_f \alpha_g u_r) = \alpha_f \nabla\cdot u - \alpha_f\left(\frac{\dot{\rho}}{\rho_f} - \frac{\dot{\rho}}{\rho_g}\right) + \frac{\dot{\rho}}{\rho_f} \tag{3}$$

Continuity equation:

$$\nabla\cdot u = \frac{S}{\rho_f} - \frac{S}{\rho_g} \tag{4}$$

Momentum equation:

$$\frac{\partial(\rho u)}{\partial t} + \nabla(\rho u u) = -\nabla P + \nabla\cdot\left[\mu\left(\nabla u + \nabla u^T\right)\right] + \rho\vec{g} + \sigma\kappa(\alpha)\boldsymbol{n}|\nabla\alpha|\frac{2\rho}{\rho_g + \rho_f} \tag{5}$$

Energy equation:

$$\frac{\partial(\rho C_p T)}{\partial t} + \nabla\cdot(\rho C_p u T) - \nabla\cdot(k_{eff}\nabla T) = Q \tag{6}$$

In the volume fraction and continuity equations, S is the mass source term, which determines how much mass is changed due to phase change. The last term of the volume fraction equation, $\nabla\cdot(\alpha_f\alpha_g u_r)$, is a term used to avoid any numerical divergence while retaining mass conservation during the calculation. This term also contributes to achieving a higher interface resolution [36]. Term u_r, which is defined as $u_f - u_g$, is a relative velocity designated as the compression velocity. The continuum surface force (CSF) model developed by Brackbill [37] was adopted to consider surface tension at the interface, as shown in the last term of the RHS in the momentum equation. The curvature of the interface was defined using the gradient of a volume fraction. Herein, we adopted the Ferrari and Lunati models [38] to define the curvature of the interface (κ) to prevent any large spatial oscillation.

$$\kappa(\alpha) = -(\nabla\cdot\boldsymbol{n}) = -\left(\nabla\cdot\frac{\nabla a}{|\nabla\alpha|}\right) \tag{7}$$

In Eq. (6), Q is the heat transfer term in accordance with the mass

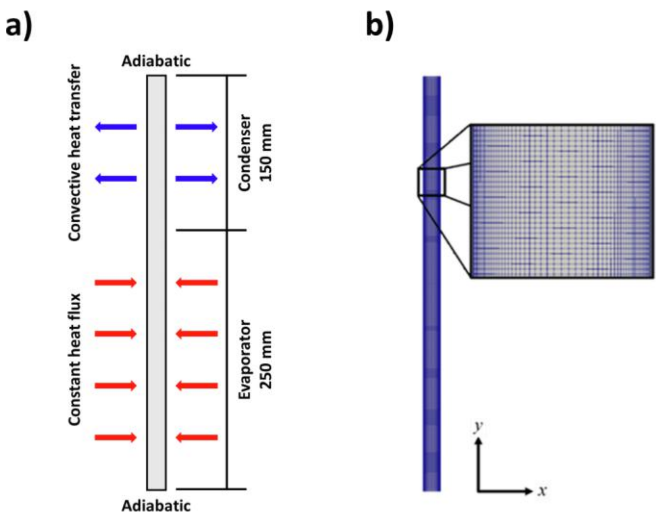

Fig. 2. Schematic representation of the computational domain.

transfer due to the phase change.

Implementing an appropriate phase change model in a two-phase simulation is very important since it defines how much mass is transferred due to the phase change and determines the corresponding surface temperature and heat transfer rate. Several phase change models have been proposed, including the Lee model [24], the Schrage model [39], the sharp-interface model [40], and the energy balance model [41]. Among these models, the Lee model has gained more popularity due to its simplicity and relative ease of implementation with commercial CFD software. Herein, we adopted the Lee model to determine the mass transfer rate, and the corresponding energy transfer can be determined as follows:

$$S_g = r_c \alpha_g \rho_g \frac{(T - T_{sat})}{T_{sat}} \text{ for condensation } (T < T_{sat}) \tag{8}$$

$$S_f = r_e \alpha_f \rho_f \frac{(T - T_{sat})}{T_{sat}} \text{ for evaporation } (T > T_{sat}) \tag{9}$$

$$Q_g = S_g h_{fg} \text{ for condensation } (T < T_{sat}) \tag{10}$$

$$Q_f = S_f h_{fg} \text{ for evaporation } (T > T_{sat}) \tag{11}$$

Here, terms S_g and S_f [kg/m^3·s] are the mass sources in accordance with the condensation and evaporation rates respectively, which is equivalent to S in Eq. (4). Terms Q_g and Q_f [W/m^3] are heat transfers caused by condensation and evaporation respectively, while r_e and r_c [s^{-1}] are mass transfer intensity factors for condensation and evaporation, respectively. The mass transfer intensity factor is an empirical constant whithin the Lee model and is related to the phase change rate. A higher mass transfer intensity factor would increase the evaporation or condensation rate, and its value is empirically selected according to the problem being solved.

The properties in Eq. (5) and Eq. (6), are determined from the following volume-averaged equations:

$$\rho = \alpha_f \rho_f + (1 - \alpha_f) \rho_g \tag{12}$$

$$\mu = \alpha_f \mu_f + (1 - \alpha_f) \mu_g \tag{13}$$

$$C_P = \alpha_f C_{P,f} + (1 - \alpha_f) C_{P,g} \tag{14}$$

$$k_{eff} = \alpha_f k_f + (1 - \alpha_f) k_g \tag{15}$$

3.2. Computational domain and boundary conditions

In this study, we used a two-dimensional computational domain for the TPCT simulations (Fig. 2). This computational domain consisted of a fluid domain with a size of 17 × 400 mm^2. The solid region was not considered, because the lateral spreading effect of the solid region was negligible due to it being relatively thin (1 mm).

A nonslip boundary condition was applied for all walls, adiabatic conditions were applied for both top and bottom walls, and a constant heat flux was used for the evaporator wall. In addition, a convective heat transfer condition with a heat transfer coefficient of 8.9 kW/m^2/K and an ambient temperature of 302.6 K was applied to the condenser wall. The wall temperature of the TPCT reached a steady state at t = 20 s, although the mass transfer rates of evaporation and condensation vary corresponding to iteration (Fig. S1). Then the time-averaged wall temperature for 30–60 s was used to compare the experimental data and simulation results. After confirming T_{sat} at the steady state in the first simulation, an initial T_{sat} was adopted as the confirmed T_{sat} in the first simulation. We also set the temperature of the liquid and vapor phases with deviations of − 0.1 and + 0.1 °C from T_{sat}, respectively, to reduce the computational cost required to reach the steady state. This method of setting the initial conditions for rapid steady-state convergence can also be found in Kim *et al.* [31].

The mesh independency was tested with four different meshes (36 k, 42 k, 48 k, and 51 k), and the averaged wall temperatures at the evaporator and condenser walls were compared. Mass transfer intensity factors of $r_c = 0.05$ s^{-1} and $r_e = 10 \times 10^4$ s^{-1} were adopted. No significant difference in wall temperature was observed between 48 k and 51 k; hence, 48 k meshes were adopted to minimize computational cost. With a Ryzen R9 5900X CPU, NVIDIA GeForce RTX 3060 GPU and DDR4 128 GB memory, a single case can take up to seven days to achieve 60 s of transient time period. Detailed mesh-independent test results are provided in Supporting Information (Fig. S2).

3.3. Solution strategy and thermophysical properties

Herein, we propose determining T_{sat} based on ρ_g in the TPCT. Since the TPCT is a closed system, T_{sat} is actively adjusted with ρ_g changes, Therefore, we can incorporate T_{sat} changes in accordance with the evaporation and condensation rates. Hence, ρ_g and the corresponding T_{sat} can be determined as follows, where superscripts *i* and *i-1* indicate the current and previous iterations, respectively:

$$\rho_g^i = \rho_g^{i-1} + (m_e^{i-1} - m_c^{i-1}) / v_g, \tag{16}$$

$$T_{sat} = 386.74 \times \rho_g^{0.058} - 10. \tag{17}$$

At each iteration, m_e and m_c represent the overall mass of evaporation and condensation occurring within TPCT, respectively. Additionally, v_g denotes the volume of vapor in TPCT. The RHS of Eq. (16) consists of the vapor density from the previous iteration, as well as the difference in vapor density between the current and previous iterations. In Eq. (17), T_{sat} is determined from curve fitting the thermophysical properties obtained by NIST REFPROP [42]. This equation provided a ± 1% difference for the temperature range where the experiment was conducted (T_{sat} = 280–350 K).

The phase change model was implemented in OpenFOAM v2106 by modifying the embedded interCondensatingEvaporatingFoam solver. The governing equations were discretized using the finite volume and VOF methods, while pressure–velocity coupling was conducted using the PIMPLE algorithm. The pressure implicit with splitting of operator (PISO) loop was inserted in the semi-implicit method for pressure-linked equations (SIMPLE) algorithm. Furthermore, the multidimensional universal limiter for explicit solution (MULES), which could restrict the volume fraction, was adopted to discretize the volume fraction equation. The first- and second-order schemes were used for the equations related

Table 2
Thermophysical properties.

Properties	Liquid water	Vapor
ρ [kg/m^3]	9.92×10^2	$\rho_g^i = \rho_g^{i-1} + (m_e^{i-1} - m_c^{i-1}) / v_g$
C_p [J/kg/K]	4.18×10^3	1.93×10^3
C_v [J/kg/K]	4.08×10^3	1.45×10^3
κ [W/m/K]	6.26×10^{-1}	1.94×10^{-2}
ν [m^2/s]	6.79×10^{-7}	2.15×10^{-4}
h [J/kg]	1.60×10^5	2.57×10^6
σ [N/m]	*T-dependent*	
T_{sat} [K]	$T_{sat} = 386.7 \times \rho_g^{0.058} - 10$	

to time and space. The convergence criteria were 10^{-6}, 10^{-6}, 10^{-8}, and 10^{-10} for the velocity, pressure, volume fraction, and temperature, respectively. The time step was 10^{-6} s, and the maximum courant number was 1. The relaxation factor was 1 for all. For a detailed solution strategy, please refer to the supporting information in Table S1. The detailed thermophysical properties used in this study are tabulated in Table 2. Surface tension was defined as temperature-dependent property (See details for supporting information Table S2 [42]); other properties are set as constant [32,43,44].

4. Results and discussion

4.1. Experimental results

Fig. 3 displays the average wall temperature of a) the evaporator section ($T_{w.e}$) and b) the condenser section ($T_{w.c}$) according to the heat flux and the FR. The wall temperature of the evaporator section varied from 310 to 340 K when $q'' = 4$–30 kW/m^2, increasing continuously as the heat flux increased. For all FR, $T_{w.e}$ tended to increase to approximately 20 K, increasing the heat flux from 4 to 30 kW/m^2. In the FR = 5%–75% group, FR = 25% displayed the lowest $T_{w.e}$ for most heat flux ranges, and FR = 5% displayed the second lowest $T_{w.e}$. The $T_{w.e}$ of FR 50% was lower than FR = 15% for heat flux under 12 kW/m^2. However, this suddenly increased to approximately 336 K for $q'' > 12$ kW/m^2 and exhibited a higher temperature compared to that of FR = 15%. The $T_{w.e}$ of FR = 75% exhibited a different trend than the other FRs. For example, $T_{w.e}$ was 328 K for 4 kW/m^2 (the second highest value), followed by 335 K for 30 W/m^2. However, the slight increase of q'' from 4 to 8 kW/m^2 caused a rapid decrease in $T_{w.e}$ of almost 10 K due to the boiling incipience at 8 kW/m^2 for FR 75%. This sudden temperature reduction was not observed in other FRs because boiling incipience occurs at $q'' < 4$ kW/m^2. In general, FR = 25% exhibited the optimum performance for most of heat flux conditions, while FR = 50% displayed the worst performance in this study. This result was because vigorous liquid fluctuation (which occurs with low FR values) caused a continuous supply of liquid to the evaporator, preventing local dry-out [45]. However, too low an FR value can result in poor performance due to local dry-out, which is caused by a low supply to the evaporator. The 25% FR had a good balance between the space for vapor and the liquid supply on the evaporator, resulting the optimum performance for the TPCT in this study. However, as the FR increased, the available space for the vapor to rise diminished, making it difficult for the vapor to escape, resulting in the formation of a vapor slug. This vapor slug could disrupt the downward flow of liquid, leading to relatively poor performance at an FR 50%.

Interestingly, $T_{w.c}$ increased as heat flux increased, which was remarkably similar to that of $T_{w.e}$. Moreover, $T_{w.c}$ of all the FRs was approximately 304 K at $q'' = 4$ kW/m^2, increasing to 10–13 K at $q'' = 30$ kW/m^2. In addition, $T_{w.c}$ increased by 16 K for FR 15%, while FR 25% took the lowest $T_{w.c}$ at $q'' = 12$–20 kW/m^2. After FR 25%, FR 5%, 15%, and 75% followed, which had similar $T_{w.c}$ values, except for FR 50%. Here, FR 50% exhibited a significant increment of $T_{w.c}$ at $q'' =16$–20 kW/m^2.

Fig. 4 demonstrates the effect of heat flux on the wall temperature of each installed thermocouple location with FR ranging from 5% to 75%. The difference between the wall temperatures of the evaporator section increased with increasing heat flux and was up to 14.5 K for the highest heat flux of $q'' = 30$ kW/m^2 while a relatively small difference was observed for low heat flux.

The wall temperature of the condenser section varied from 302 to 320 K with $q'' = 4$–30 kW/m^2 and continuously increased with increasing heat flux, similar to the temperature change of the evaporator section. The main reason for increasing wall temperature in the condenser section was that increasing heat flux resulted in increased pressure, leading to increased T_{sat} in the TPCT.

Fig. 5 displays the overall thermal performance of the TPCT according to heat flux variations for each FR. As shown in the figure, R_{th} exhibited very similar values (0.06–0.11 K/W) at a relatively high heat flux range of $q'' = 16$–30 kW/m^2, and converged to 0.05 K/W at the highest heat flux of $q'' = 30$ kW/m^2. Moreover, R_{th} exhibited increasing divergence with different FRs at low heat flux ranges of $q'' = 4$–12 kW/m^2. In particular, R_{th} varied from 0.08 K/W for FR = 25% to 0.46 K/W for FR = 75% at the lowest $q'' = 4$ kW/m^2. Here, R_{th} was mainly dominated by the change of $T_{w.e}$, since the change of $T_{w.c}$ was relatively small compared to $T_{w.e}$. FR 25% showed the minimum R_{th} values for most heat flux ranges except for $q'' = 16$–20 kW/m^2, where FR 75% exhibited the minimum thermal resistance. The R_{th} of FR 75% was significantly higher at 0.46 K/W than other FRs at $q'' = 4$ kW/m^2, as boiling had not yet occurred. However, this decreased sharply to 0.14 K/W after boiling started at $q'' = 8$ kW/m^2 and maintained a low thermal resistance for

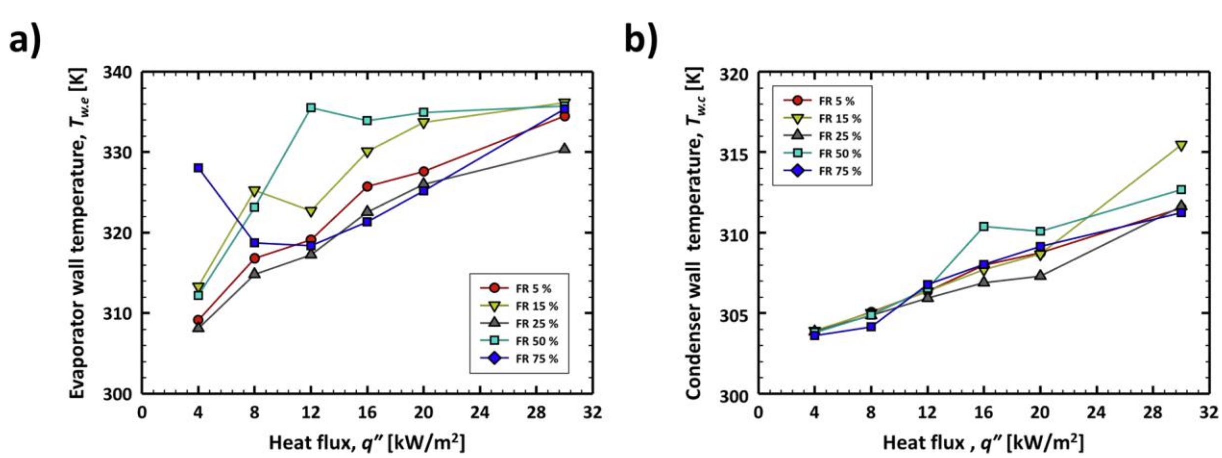

Fig. 3. Experimentally determined average wall temperature for five different filling ratio of 5–75%. The average wall temperature in a) the evaporator section and b) the condenser section.

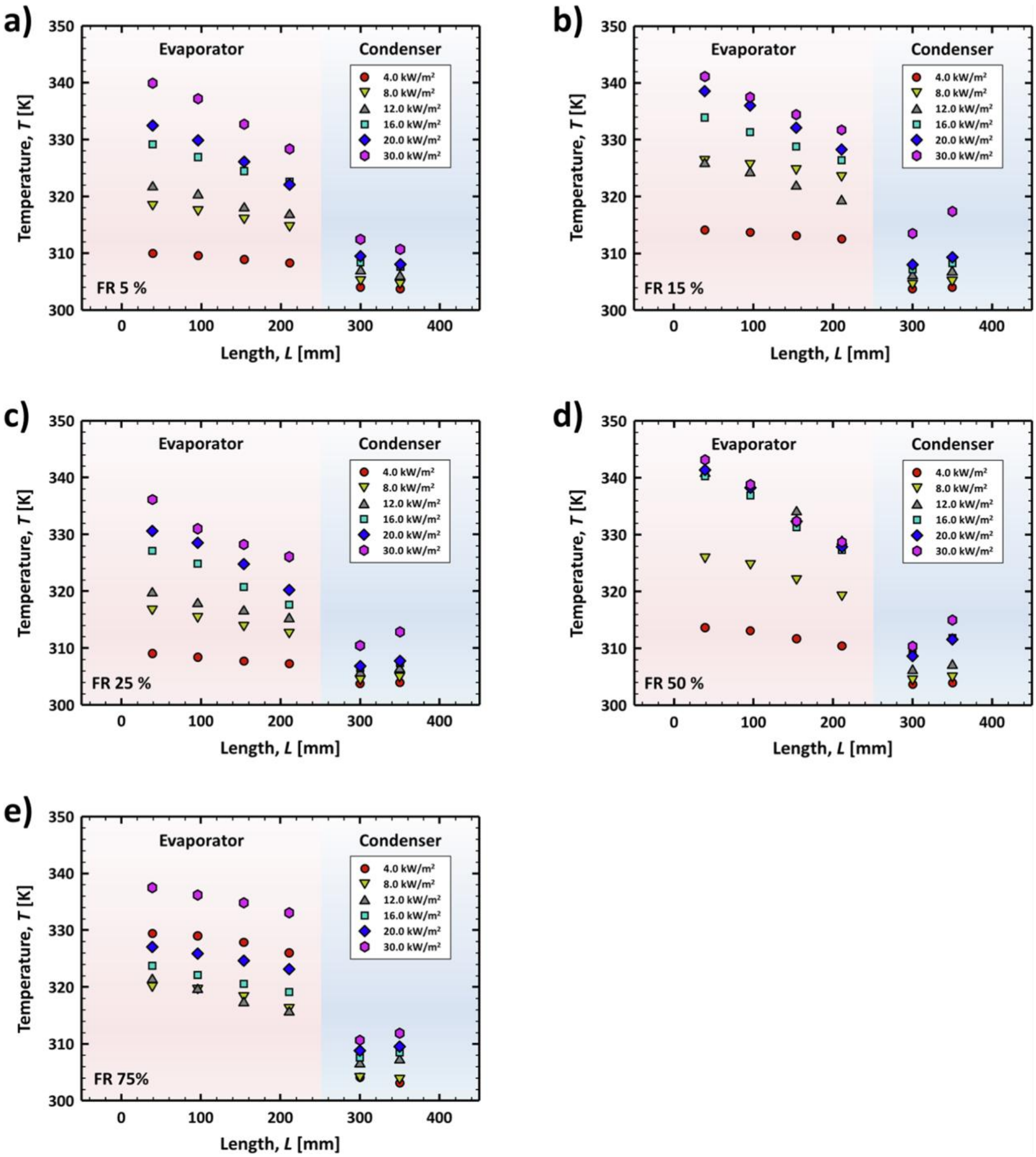

Fig. 4. Experimental results of temperature distribution by filling ratio. a) FR = 5%, b) FR = 15%, c) FR = 25%, d) FR = 50%, and e) FR = 75%.

high heat flux ranges of $q'' > 20$ kW/m^2.

4.2. Computational results

4.2.1. Thermal performance prediction of TPCT

In this section, the phase change simulation was implemented to investigate the temperature distribution and thermal performance using a model with T_{sat} considering the mass balance based on the experimental data. A specific experimental case of FR 75% under 8 kW/m^2 was used to minimize computational cost, since different operating regimes (including before and after boiling incipience) can be compared with increasing heat flux values. Detailed values of the experimental data used for validation are tabulated in Table 3.

A comparison between the experimental data and computational results is displayed in Fig. 6. The mass transfer intensity factors for $r_e = 0.025$–0.075 s^{-1} and $r_c = 5 \times 10^4$ to 100×10^4 s^{-1} were used for the simulation, and $r_e = 0.025$ s^{-1} and $r_c = 50 \times 10^4$ s^{-1} were used for the comparison since this provided the best predictive accuracy. Overall, the computational results were in good agreement with the experimental data. Most temperature predictions exhibited relatively small temperature deviations of 0.5 K at $T_{e.4}$, with the largest temperature deviation of 2.4 K at $T_{e.1}$. The temperature distribution at the bottom of the evaporator section was remarkably similar to the experimental data. The temperatures in the condenser section were also in good agreement with the minimum and maximum temperature deviations of 1.1 K at $T_{c.1}$ and 2.4 K at $T_{c.2}$, respectively. The temperature of the condenser section also exhibited reasonable agreement with the experimental data, although it varied slightly with respect to the y-direction due to droplets on the

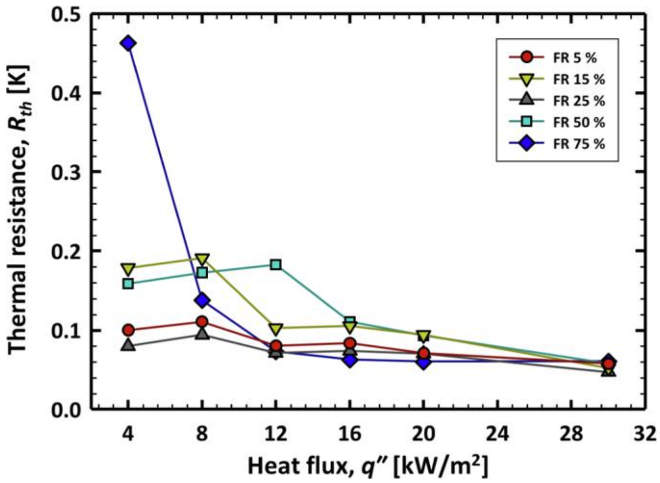

Fig. 5. Variations of total thermal resistance with heat flux for five different filling ratios.

Table 3
Detailed thermal information of experimental data for validation.

Data		L [mm]	T [K]	T_w [K]	R_{th} [K/W]
Condenser	$T_{c.1}$	350	304.0	304.1	0.138
	$T_{c.2}$	300	304.3		
Evaporator	$T_{e.1}$	211	316.5	318.8	
	$T_{e.2}$	154	318.5		
	$T_{e.3}$	96	319.8		
	$T_{e.4}$	39	320.3		

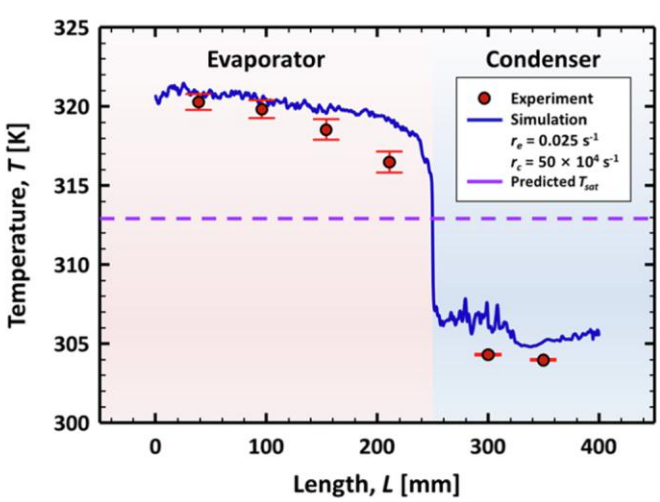

Fig. 6. Axial variations of experimental and computed wall temperatures.

Table 4
Comparison between experimental data and computational results.

Data		L [mm]	T_{exp} [K]	$T_{CFD.ref}$ [K]	ΔT [K]
Condenser	$T_{c.1}$	350	304.0	305.1	1.1
	$T_{c.2}$	300	304.3	306.7	2.4
Evaporator	$T_{e.1}$	211	316.5	318.9	2.4
	$T_{e.2}$	154	318.5	320.1	1.6
	$T_{e.3}$	96	319.8	320.5	0.7
	$T_{e.4}$	39	320.3	320.8	0.5

condenser wall. A dotted line in Fig. 6 shows the T_{sat} obtained from Eq. (17). The calculated T_{sat} value was located between the temperatures of the evaporator and condenser sections, which implied a reasonable temperature prediction. Detailed information on the temperatures of both the experimental and computational data is tabulated in Table 4. The computational data with T_{sat} considering the mass balance was also compared with computational data having a constant T_{sat}, which was commonly used in the previous literature, as displayed in Supporting Information (Fig. S3).

Fig. 7(a) depicts the computed contour plots for a volume fraction with $r_e = 0.025$ s^{-1} and $r_c = 50 \times 10^4$ s^{-1}, which demonstrated the optimum predictive accuracy. In the figure, the elapsed time between consecutive images was 0.25 s, the blue color represents the liquid phase (with a volume fraction of zero), while the vapor phase is expressed as red. The bubble developed from the lower evaporator section and ascended towards the condenser section due to the buoyancy force. Then, it was condensed to a liquid by releasing the heat onto the condenser wall. Fig. 7(b) displays the sequential volume fraction images focused on the condenser wall for $r_e = 0.025$ s^{-1} and $r_c = 50 \times 10^4$ s^{-1}. Consecutive images were captured with a time interval of 0.05 s. Here, relatively small liquid droplets were observed in the upper region of the condenser wall. In contrast, a bigger and longer liquid film was formed in the bottom region of the condenser wall with the aid of merging droplets. Fig. 7(c) displays the volume fraction and corresponding temperature contour plots of the bubble developed in the evaporator section. The temperature of the bubble inside was approximately 318 K, which was sufficiently high to be vaporized ($>T_{sat}$), while the temperature of the bubble outside was lower than 310 K. A temperature relatively higher than T_{sat} was maintained due to several small bubbles between the slug, which were separated from the tail edge of the bubble.

4.2.2. Effect of mass transfer intensity factor on the flow pattern

In this section, we investigate the effect of the mass transfer intensity factor of the Lee model on the flow pattern of the TPCT. Here, 12 cases were simulated to gain a better understanding of the volume fraction changes with mass transfer intensities spanning r_e = 0.025–0.075 s^{-1} and $r_e = 5 \times 10^4$ to 100×10^4 s^{-1}. Details of the simulation cases are tabulated in Table 5.

Fig. 8 displays the effect of mass transfer intensity factor on the flow pattern of condensation. Overall, the flow pattern was seriously affected by r_c and clearly exhibited more condensed liquid as r_c increased. Moreover, dropwise condensation was observed at a relatively lower value of $r_c = 5 \times 10^4$ to 50×10^4 s^{-1}, and the droplet size increased by reinforcing condensation when r_c increased. As the condensation rate increased for relatively larger values of $r_c = 100 \times 10^4$ s^{-1}, the liquid droplets were sufficiently large to form a film; hence, film condensation was observed over the entire condensation region. At a fixed r_c, the droplet size of dropwise condensation slightly decreased with increasing r_e, although there was no significant difference in the volume fraction of the condensation region. In addition, although the r_e increment reinforced the boiling, the incremental step of r_e was too insignificant to make a remarkable change in the boiling flow pattern. Therefore, r_c did not affect the boiling flow pattern. For relatively larger values of r_e = 0.075 s^{-1} and $r_c = 50 \times 10^4$ to 100×10^4 s^{-1}, temporal instability was observed with fluctuating temperatures.

4.2.3. Effect of mass transfer intensity factor on thermal performance prediction

We also investigated changes in thermal performance according to the mass transfer intensity factor, as presented in Table 5, while the corresponding simulation results for $T_{w.e}$, $T_{w.c}$, and R_{th} are summarized in Table 6. Here, $T_{w.e}$ was distributed over a wide range (317.9–336.1 K), while $T_{w.c}$ was in a relatively narrow range (305.9–309.5 K) for changes in r_e = 0.025–0.075 s^{-1} and $r_c = 5 \times 10^4$ to 100×10^4 s^{-1}. Moreover, $T_{w.e}$ and $T_{w.c}$ increased as either r_e or r_c increased and decreased when r_e or r_c decreased. In particular, $T_{w.e}$ substantially decreased as r_c increased from

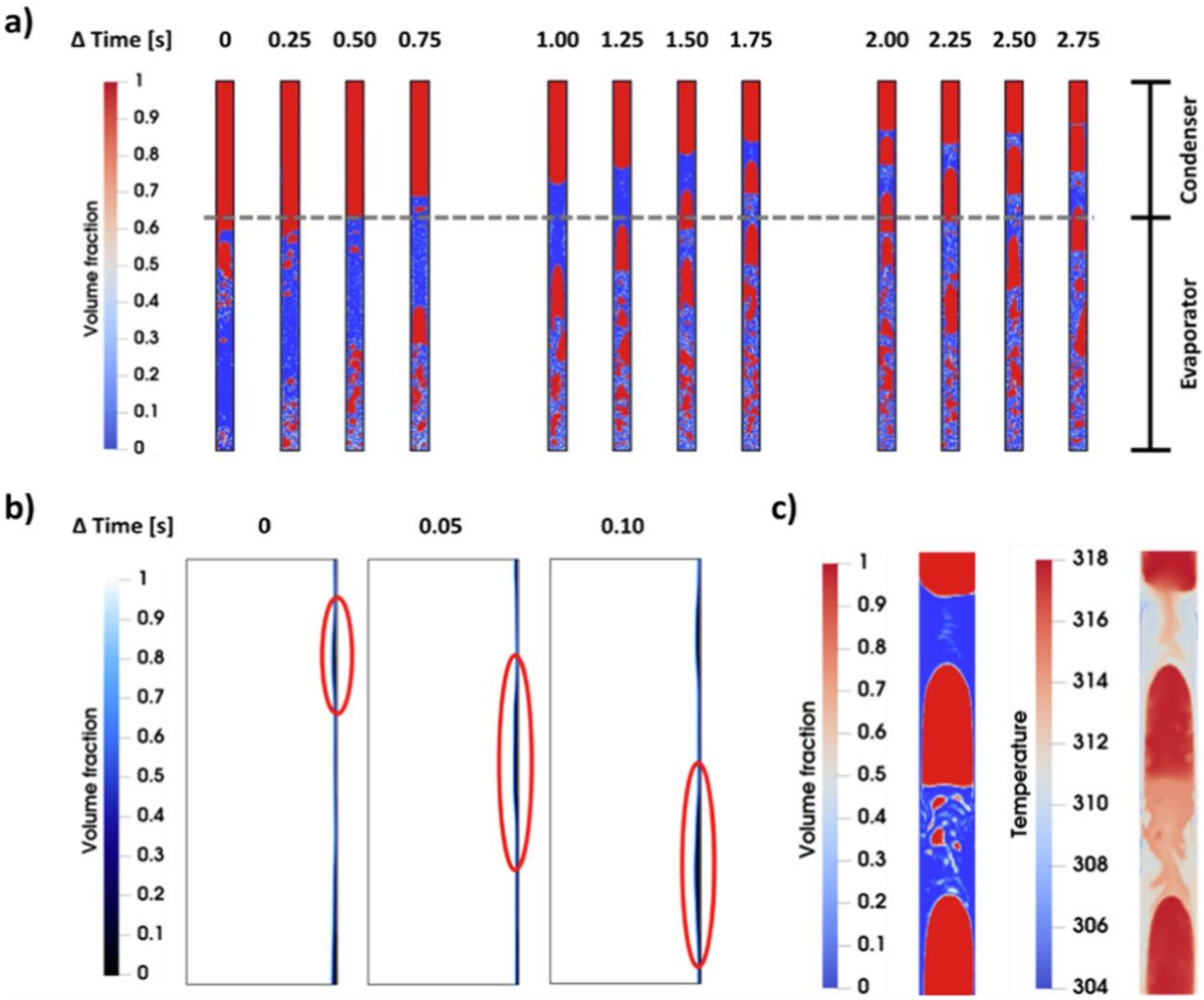

Fig. 7. Computed flow visualization contour plots. a) volume faction of vapor at different time instants b) condensation flow c) volume fraction and temperature of the bubble.

Table 5
Simulation matrix by a mass transfer intensity factor.

	Mass transfer intensity factor of condensation				
	r_e [s^{-1}]	r_c [s^{-1}] 5 × 10^4	10 × 10^4	50 × 10^4	100 × 10^4
Mass transfer intensity factor of evaporation	0.025	Case 1	Case 2	Case 3 (Ref.)	Case 4
	0.05	Case 5	Case 6	Case 7	Case 8
	0.075	Case 9	Case 10	Case 11	Case 12

5×10^4 s^{-1} to 10×10^4 s^{-1}. However, the decrement weakened when r_c changed from 10×10^4 s^{-1} to 50×10^4 s^{-1}, and $T_{w.e}$ increased with further changes in r_e from 50×10^4 s^{-1} to 100×10^4 s^{-1}. |In addition, $T_{w.c}$ displayed a remarkably similar trend to that of $T_{w.e}$ with changes in r_c. Although $T_{w.c}$ mostly decreased as r_c increased, the difference was relatively small compared to the changes in $T_{w.e}$, which mainly increased with increasing r_e. A larger increase was observed in $T_{w.e}$ for a small r_c of 5×10^4 s^{-1} compared to that of a large r_c of 100×10^4 s^{-1}. However, $T_{w.e}$ slightly decreased with increasing r_e at $r_c = 10 \times 10^4$ s^{-1}.

Fig. 9 demonstrates the changes in T_{sat}, $T_{w.e}$, and $T_{w.c}$ with changes in r_c and r_e. The trend is described under a constant r_c and variable r_e in Fig. 9(a), and a constant r_e, and variable r_c in Fig. 9(b). First, T_{sat} was the most dominant factor for $T_{w.e}$, which increased with increasing T_{sat}, while $T_{w.e}$ decreased with decreasing T_{sat}. When T_{sat} was high, boiling incipience was delayed; thus, most applied heat from the evaporator section increased $T_{w.e}$ by adding sensible heat to the working fluid. On the one hand, boiling incipience occurred at low temperatures when T_{sat} was low, meaning applied heat was used as latent heat by maintaining a low $T_{w.e}$. Second, $\Delta T_{w.e}$ ($T_{w.e}$ - T_{sat}) decreased with increasing r_e. Moreover, increased r_e accelerated evaporation; hence, heat transfer was also promoted. Table 7 presents the values of $\Delta T_{w.e}$ calculated from each case. Cases 1–4 had an r_e of 0.025 s^{-1} and exhibited $\Delta T_{w.e}$ values in the range 6.2–6.8 K, with an average $\Delta T_{w.e}$ value of 6.6 K. Cases 5–8 had an r_e of 0.05 s^{-1} produced $\Delta T_{w.e}$ values in the range 3.6–4.6 K, with an average $\Delta T_{w.e,}$ of 4.2 K. For Cases 9 and 10, r_e was 0.075 s^{-1}, producing respective $\Delta T_{w.e}$ values of 3.2 and 3.6 K with $\Delta T_{w.e.avg}$ of 3.4 K. In summary, when r_e increased from 0.025 to 0.075 s^{-1}, $\Delta T_{w.e.avg}$ decreased from 6.6 to 3.4 K.

Although $T_{w.c}$ slightly increased with increasing r_e, a much lower increase was observed compared to $T_{w.e}$. As mentioned in Fig. 4, increasing heat flux resulted in a higher T_{sat} in the TPCT. However, a fixed coolant temperature in the condenser section produced a relatively small temperature increment compared to that of the evaporator section. Therefore, $T_{w.c}$ barely changes with r_c, while $T_{w.e}$ changes substantially with r_e.

Finally, T_{sat} was affected by both r_e and r_c, with T_{sat} tending to increase with increasing r_e due to promoted boiling mass transfer, resulting in an increase in ρ_g. In contrast, increasing r_c resulted in decreasing

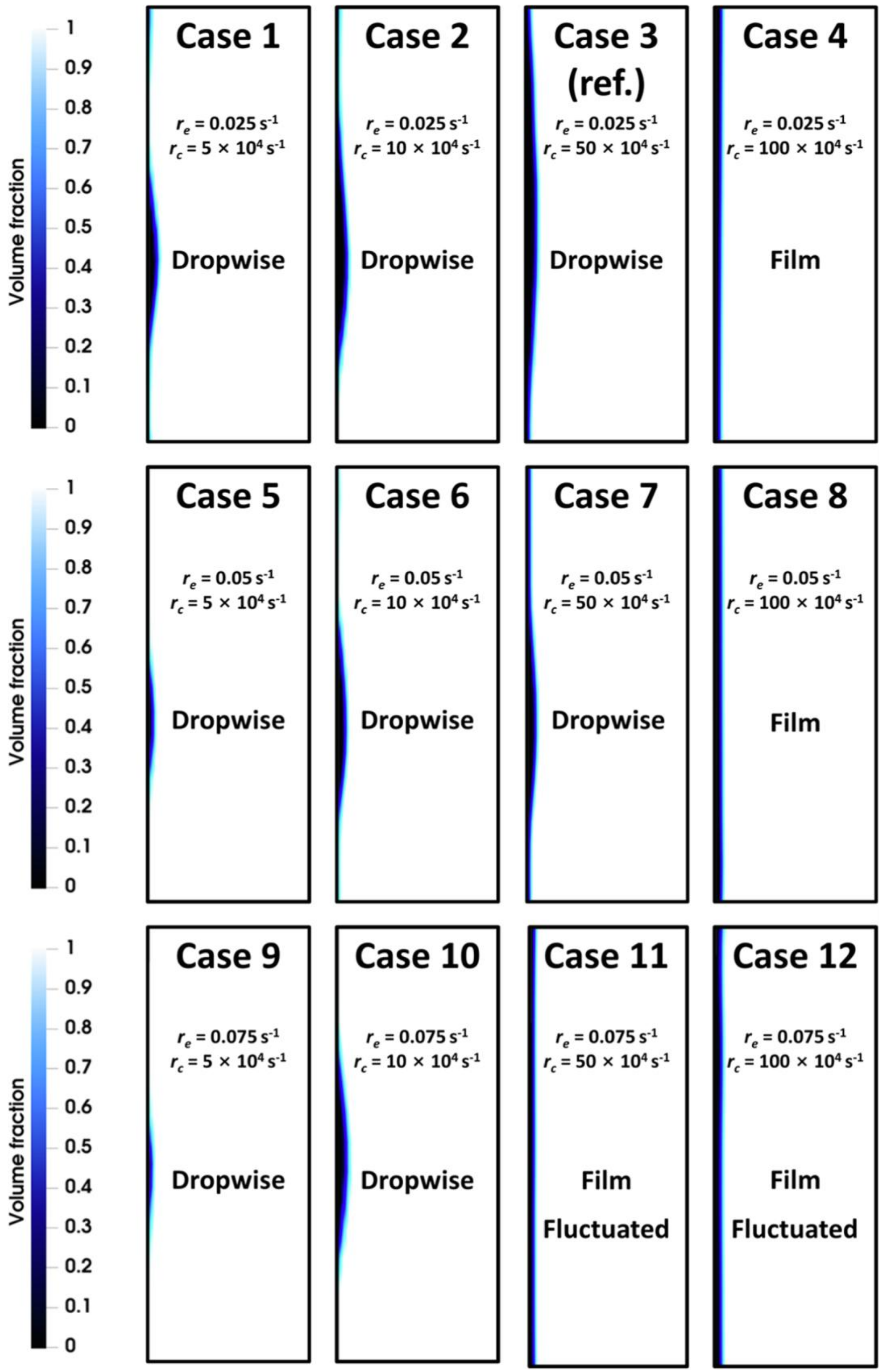

Fig. 8. Effect of mass transfer intensity factors on condensation region.

T_{sat}, since decreasing ρ_g facilitated more condensation. However, T_{sat} started to decrease as r_c increased to 100×10^4 s^{-1}. The main reason for T_{sat} decreasing was because the flow pattern changed from dropwise condensation to film condensation with increasing r_c from 50×10^4 s^{-1} to 100×10^4 s^{-1}. As described in Fig. 8, the flow pattern on the condenser wall was expressed as dropwise condensation with an r_c of 5×10^4 to 50×10^4 s^{-1}, while the flow pattern transformed to film condensation with an r_c of 100×10^4 s^{-1}. As a result, the film

Table 6
Numerical results of simulation matrix.

		Mass transfer intensity factor of condensation			
	r_e [s^{-1}]	r_c [s^{-1}]			
		5×10^4	10×10^4	50×10^4	100×10^4
Mass transfer intensity factor of evaporation	0.025	**Case 1** $T_{w.e}$ = 327.5 K $T_{w.c}$ = 306.6 K R_{th} = 0.197 K/W	**Case 2** $T_{w.e}$ = 323.7 K $T_{w.c}$ = 306.1 K R_{th} = 0.166 K/W	**Case 3 (Ref.)** $T_{w.e}$ = 319.7 K $T_{w.c}$ = 305.9 K R_{th} = 0.130 K/W	**Case 4** $T_{w.e}$ = 321.4 K $T_{w.c}$ = 306.4 K R_{th} = 0.142 K/W
	0.05	**Case 5** $T_{w.e}$ = 330.7 K $T_{w.c}$ = 308.1 K R_{th} = 0.214 K/W	**Case 6** $T_{w.e}$ = 321.8 K $T_{w.c}$ = 306.2 K R_{th} = 0.147 K/W	**Case 7** $T_{w.e}$ = 321.3 K $T_{w.c}$ = 307.0 K R_{th} = 0.135 K/W	**Case 8** $T_{w.e}$ = 322.2 K $T_{w.c}$ = 306.8 K R_{th} = 0.145 K/W
	0.075	**Case 9** $T_{w.e}$ = 336.1 K $T_{w.c}$ = 309.5 K R_{th} = 0.251 K/W	**Case 10** $T_{w.e}$ = 322.1 K $T_{w.c}$ = 306.6 K R_{th} = 0.146 K/W	**Case 11** *Fluctuated*	**Case 12** *Fluctuated*

contributed to an increase in the R_{th} of condensation, disturbing effective condensation heat transfer.

Fig. 10 presents the temperature distribution along the TPCT depending on the mass transfer intensity factor. The temperature remained almost constant at 0–200 mm from the bottom of the TPCT. However, it started to decrease at lengths of 200–250 mm due to the cooling liquid supply from the condenser section. In the condenser section, the temperature varied spatially with the presence of liquid droplets, although it mainly remained constant. Increasing r_c caused lower evaporator temperature, while the condenser temperature remained almost constant. The evaporator wall temperature increased with increasing r_e, although this barely affected the condenser wall temperature.

5. Conclusions

In this study, we investigated the temperature distribution and thermal performance of a 400 mm TPCT using an experimental method. The temperature distribution and thermal performance trends were analyzed under different conditions, including heat flux (4–30 kW/m^2)

Table 7
Temperature difference by mass transfer intensity factor of evaporation.

Case	r_e [s^{-1}]	r_c [s^{-1}]	$T_{w.e}$ [K]	T_{sat} [K]	$\Delta T_{w.e}$ [K]	$\Delta T_{w.e.avg}$ [K]
1	0.025	5×10^4	327.5	321.3	6.2	6.6
2		10×10^4	323.7	316.9	6.8	
3		50×10^4	319.7	312.9	6.8	
4		100×10^4	321.4	315.0	6.4	
5	0.05	5×10^4	330.7	327.1	3.6	4.2
6		10×10^4	321.8	317.4	4.4	
7		50×10^4	321.3	316.7	4.6	
8		100×10^4	322.2	317.9	4.3	
9	0.075	5×10^4	336.1	332.9	3.2	3.4
10		10×10^4	322.1	318.5	3.6	

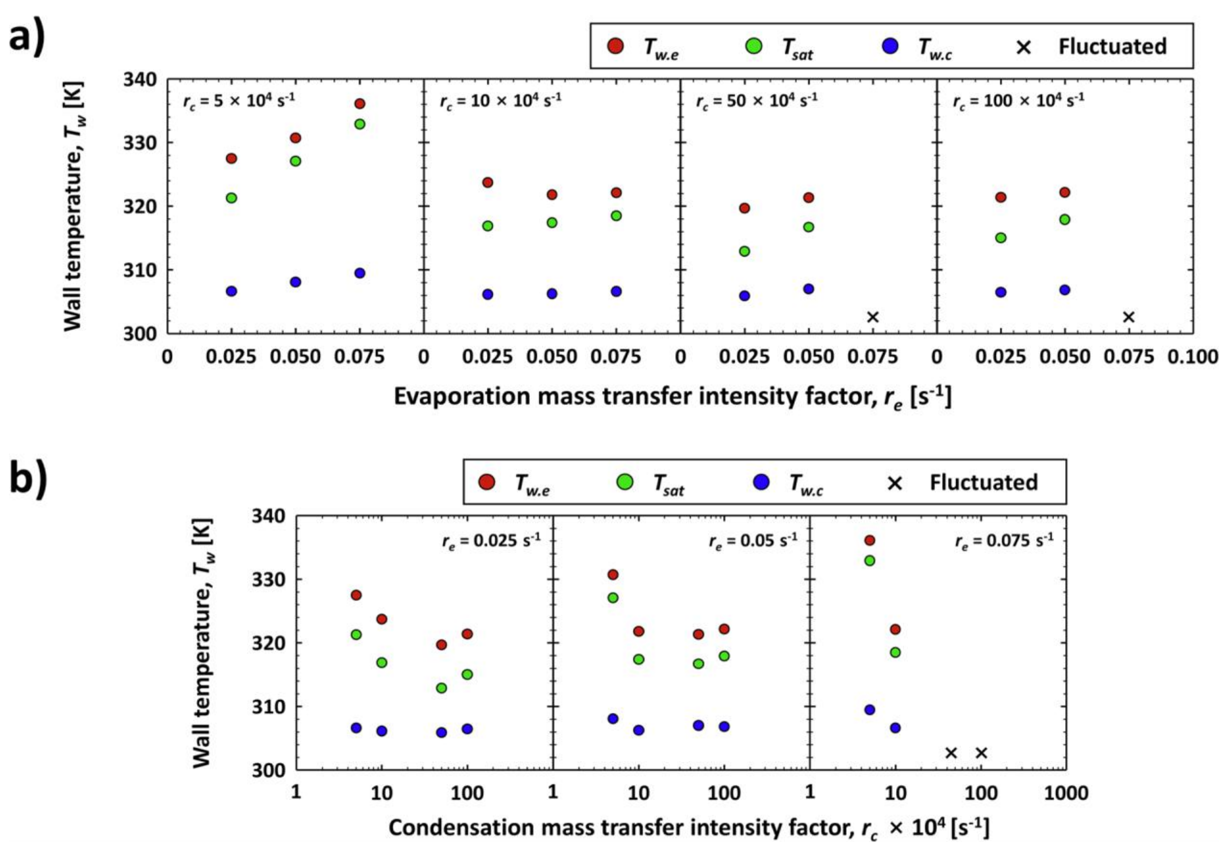

Fig. 9. Effect of mass transfer intensity factor on wall temperature in the TPCT. Variations of wall temperature with a) r_c of 5×10^4 – 100×10^4 and b) r_e of 0.025 – 0.075.

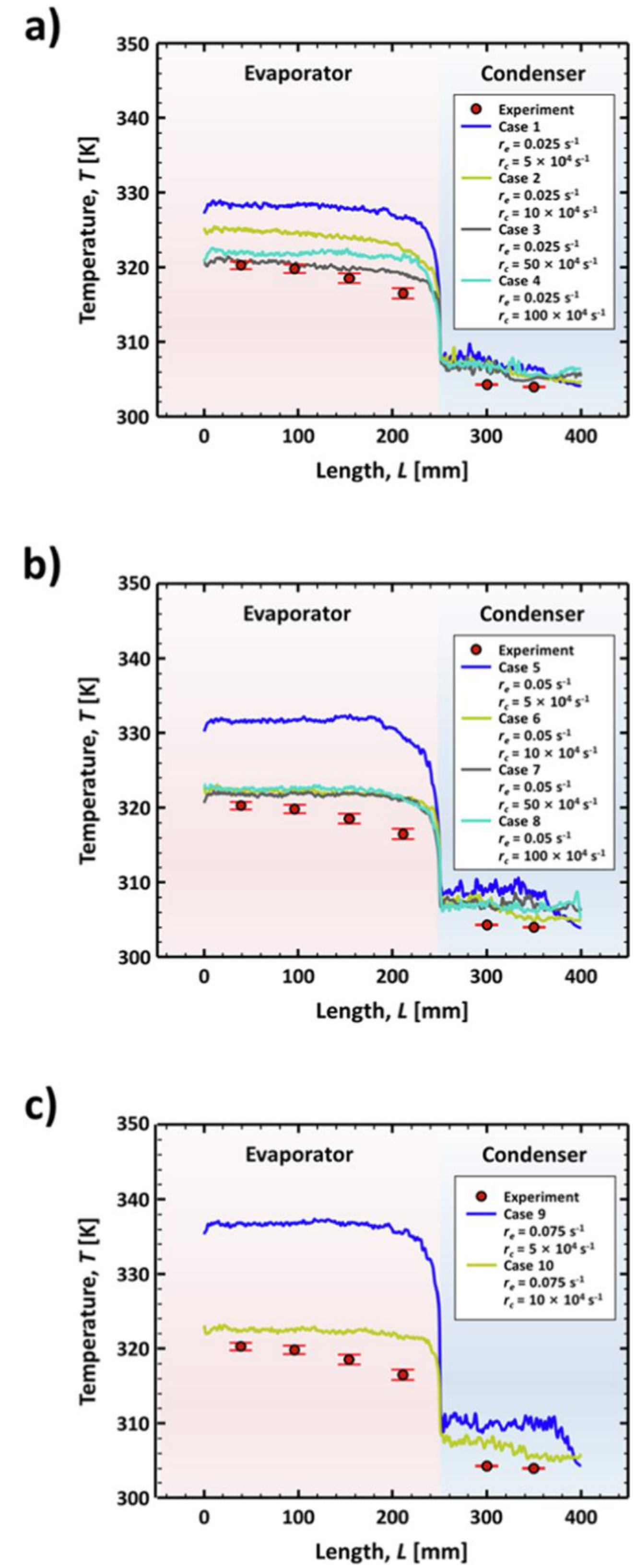

Fig. 10. Axial variations of experimental and computed wall temperature. a) Cases 1–4, b) Cases 5–8, and c) Cases 9 and 10.

and FR (5%–75 %). In addition, a new computational model was employed to predict the thermal performance and visualize the flow patterns in the TPCT. The model considered the mass balance in the TPCT and set the T_{sat} and the ρ_g corresponding to mass balance to improve the predictive accuracy of the phase-change simulations. The experimental data validated the computational results and the effect of the mass transfer intensity factor on the flow pattern and thermal performance of TPCT was investigated. The key findings from this study are as follows:

1. The thermal performance of a TPCT was experimentally determined. Different FRs of 5%–75 % were tested with a wide range of heat flux values ($q'' = 4$–30 kW/m^2). Overall, FR 25% exhibited the best thermal performance having the lowest $T_{w.e}$, $T_{w.c}$, and R_{th} for the most heat flux conditions. Otherwise, FR 50% exhibited the worst thermal performance, having the highest $T_{w.e}$, $T_{w.c}$, and R_{th} values. For all FRs, R_{th} decreased with increasing heat flux.
2. A new method for determining T_{sat} from the mass balance was adopted, and the computational results demonstrated superior predictive accuracy, achieving a temperature difference within ± 3 K compared to the experimental data.
3. The effect of mass transfer intensity factor on flow pattern was extensively investigated computationally. The flow pattern of condensation varied from dropwise condensation to film condensation according to r_c. However, no significant change was observed in the boiling flow pattern with different mass transfer intensity factors.
4. The trends of $T_{w.e}$, $T_{w.c}$, and T_{sat} were investigated using the mass transfer intensity factor. Here, $T_{w.e}$ and $T_{w.c}$ were affected by r_e, r_c, and T_{sat}. Therefore, the trend of T_{sat} should be interpreted by using both the mass transfer intensity factor and the flow pattern in TPCTs.

Declaration of Competing Interest

The authors declare that they have no known competing financial interests or personal relationships that could have appeared to influence the work reported in this paper.

Data availability

Data will be made available on request.

Acknowledgment

This work was supported by the Korea Institute of Energy Technology Evaluation and Planning (KETEP) grant funded by the Ministry of Trade, Industry & Energy, Korea. (Grant No. 20212020800270), the National Research Foundation of Korea (NRF) grant funded by the Korean government (MSIT) (No. 2021R1C1C1012119), and the Chung-Ang University Graduate Research Scholarship in 2021.

Appendix A. Supplementary material

Supplementary data to this article can be found online at https://doi.org/10.1016/j.applthermaleng.2023.121327.

References

[1] H. Jouhara, N. Khordehgah, S. Almahmoud, B. Delpech, A. Chauhan, S.A. Tassou, Waste heat recovery technologies and applications, Thermal Sci. Eng. Prog. 6 (2018) 268–289, https://doi.org/10.1016/j.tsep.2018.04.017.

[2] Y. Kim, J.S. Kim, D.H. Shin, S.M. You, J. Lee, Enhanced thermal performance of a thermosyphon for waste heat recovery: microporous coating at evaporator and hydrophobic coating at condenser, Appl. Therm. Eng. 175 (2020), 115332, https://doi.org/10.1016/j.applthermaleng.2020.115332.

[3] Y. Peng, X. Zhang, J. Liu, S. Li, Y. Mou, J. Xu, M. Chen, Waste heat recycling of high-power lighting through chips on thermoelectric generator, Energ. Conver. Manage. 243 (2021), 114329, https://doi.org/10.1016/j.enconman.2021.114329.

[4] A. Takezawa, K. Makihara, N. Kogiso, M. Kitamura, Layout optimization methodology of piezoelectric transducers in energy -recycling semi -active vibration control systems, J. Sound Vib. 333 (2014) 327–344.

[5] V. Safari, H. Abolghasemi, L. Darvishvand, B. Kamkari, Thermal performance investigation of concentric and eccentric shell and tube heat exchangers with different fin configurations containing phase change material, J. Storage Mater. 37 (2021), 102458, https://doi.org/10.1016/j.est.2021.102458.

[6] A.A. Abbasian Arani, R. Moradi, Shell and tube heat exchanger optimization using new baffle and tube configuration, Appl. Therm. Eng. 157 (2019), 113736, https://doi.org/10.1016/j.applthermaleng.2019.113736.

[7] R. Lotfi, A.M. Rashidi, A. Amrollahi, Experimental study on the heat transfer enhancement of MWNT-water nanofluid in a shell and tube heat exchanger, Int. Commun. Heat Mass Transfer 39 (2012) 108–111, https://doi.org/10.1016/j.icheatmasstransfer.2011.10.002.

[8] S. Hossen, A.M. Morshed, A. Tikadar, A.S. Salman, T.C. Paul, "Experimental investigation of heat pipe heat exchanger (HPHE) for waste heat recovery application, in: 4th Thermal and Fluids Engineering Conference, Jul. 2019, pp. 843–851.

[9] D. Jafari, A. Franco, S. Filippeschi, P. Di Marco, Two-phase closed thermosyphons: a review of studies and solar applications, Renew. Sustain. Energy Rev. 53 (2016) 575–593, https://doi.org/10.1016/j.rser.2015.09.002.

[10] W. Pei, M. Zhang, X. Wan, Y. Lai, C. Wang, Numerical optimization of the installing position for the L-shaped TPCT in a permafrost embankment based on the spatial heat control, Sol. Energy 224 (2021) 1406–1425, https://doi.org/10.1016/j.solener.2021.06.044.

[11] M. Jafari Gukeh, C. Bao, A. Mukhopadhyay, G. Damoulakis, S.K. Mazumder, C. M. Megaridis, Air-cooled hybrid vapor chamber for thermal management of power electronics, Appl. Therm. Eng. 224 (2023), 120081, https://doi.org/10.1016/j.applthermaleng.2023.120081.

[12] D. Kong, E. Jung, Y. Kim, V.V. Manepalli, K.J. Rah, H.S. Kim, et al., An additively manufactured manifold-microchannel heat sink for high-heat flux cooling, Int. J. Mech. Sci. 248 (2023), 108228, https://doi.org/10.1016/j.ijmecsci.2023.108228.

[13] S.H. Noie, M.R. Sarmasti Emami, M. Khoshnoodi, Effect of inclination angle and filling ratio on thermal performance of a two-phase closed thermosyphon under normal operating conditions, Heat Transfer Eng. 28 (4) (2007) 365–371, https://doi.org/10.1080/01457630601122997.

[14] Y. Kim, J.S. Kim, D.H. Shin, J.H. Seo, S.M. You, J. Lee, Effects of hydrophobic and superhydrophobic coatings of a condenser on the thermal performance of a two-phase closed thermosyphon, Int. J. Heat Mass Transf. 144 (2019), 118706, https://doi.org/10.1016/j.ijheatmasstransfer.2019.118706.

[15] M. Kaya, An experimental investigation on thermal efficiency of two-phase closed thermosyphon (TPCT) filled with CuO/water nanofluid, Eng. Sci. Technol. Int. J. 23 (2020) 812–820, https://doi.org/10.1016/j.jestch.2020.06.006.

[16] A. Alizadehdakhel, M. Rahimi, A.A. Alsairafi, CFD modeling of flow and heat transfer in a thermosyphon, Int. Commun. Heat Mass Transfer 37 (2010) 312–318, https://doi.org/10.1016/j.icheatmasstransfer.2009.09.002.

[17] A.M. Al Jubori, Q.A. Jawad, Computational evaluation of thermal behavior of a wickless heat pipe under various conditions, Case Stud. Therm. Eng. 22 (2020), 100767, https://doi.org/10.1016/j.csite.2020.100767.

[18] A. Tarokh, C. Bliss, A. Hemmati, Performance enhancement of a two-phase closed thermosyphon with a vortex generator, Appl. Therm. Eng. 182 (2021), 116092, https://doi.org/10.1016/j.applthermaleng.2020.116092.

[19] S. ed-Dîn Fertahi, T. Bouhal, Y. Agrouaz, T. Kousksou, T. El Rhafiki, Y. Zeraouli, Performance optimization of a two-phase closed thermosyphon through CFD numerical simulations, Appl. Thermal Eng. 128 (2018) 551–563, https://doi.org/10.1016/j.applthermaleng.2017.09.049.

[20] J. Yuan, C. Wang, J. Zhang, J. Ling, Z. Zhou, F. Gao, Effect of non-condensable gas on thermal characteristics in two-phase closed thermosyphon, Appl. Therm. Eng. 173 (2020), 115233, https://doi.org/10.1016/j.applthermaleng.2020.115233.

[21] D. Jafari, S. Filippeschi, A. Franco, P. Di Marco, Unsteady experimental and numerical analysis of a two-phase closed thermosyphon at different filling ratios, Exp. Therm Fluid Sci. 81 (2017) 164–174, https://doi.org/10.1016/j.expthermflusci.2016.10.022.

[22] X. Wang, Y. Wang, H. Chen, Y. Zhu, A combined CFD/visualization investigation of heat transfer behaviors during geyser boiling in two-phase closed thermosyphon, Int. J. Heat Mass Transf. 121 (2018) 703–714, https://doi.org/10.1016/j.ijheatmasstransfer.2018.01.005.

[23] P. Dhanalakota, L.K. Malla, H. Dileep, P. Sinha Mahapatra, A. Pattamatta, Effective thermal management of heat sources in sustainable energy devices using a compact flat thermosyphon, Energy Conver. Manage. 268 (2022), 116041, https://doi.org/10.1016/j.enconman.2022.116041.

[24] W.H. Lee, A pressure iteration scheme for two-phase flow modeling, in: T. N. Veziroglu (Ed.), Multiphase Transport Fundamentals, Reactor Safety, Applications, Hemisphere Publishing, Washington, DC, 1980.

[25] H. Lee, C.R. Kharangate, N. Mascarenhas, I. Park, I. Mudawar, Experimental and computational investigation of vertical downflow condensation, Int. J. Heat Mass Transf. 85 (2015) 865–879, https://doi.org/10.1016/j.ijheatmasstransfer.2015.02.037.

[26] X. Wang, H. Yao, J. Li, Y. Wang, Y. Zhu, Experimental and numerical investigation on heat transfer characteristics of ammonia thermosyhpons at shallow geothermal temperature, Int. J. Heat Mass Transf. 136 (2019) 1147–1159, https://doi.org/10.1016/j.ijheatmasstransfer.2019.03.080.

[27] K. Kafeel, A. Turan, Simulation of the response of a thermosyphon under pulsed heat input conditions, Int. J. Therm. Sci. 80 (2014) 33–40, https://doi.org/10.1016/j.ijthermalsci.2014.01.020.

[28] H. Yao, C. Yue, Y. Wang, H. Chen, Y. Zhu, Numerical investigation of the heat and mass transfer performance of a two-phase closed thermosiphon based on a modified CFD model, Case Studies in Thermal Engineering 26 (2021) 101155, https://doi.org/10.1016/j.csite.2021.101155.

[29] Y. Xiao, J.-W. Liu, J.-F. Zeng, X. Lu, Y. Tian, C.-M. Shu, Coupling effect of operational factors on heat extraction from a coal pile using a two-phase closed thermosyphon, Energy 239 (2022) 122371, https://doi.org/10.1016/j.energy.2021.122371.

[30] Z. Xu, Y. Zhang, B. Li, C.-C. Wang, Y. Li, The influences of the inclination angle and evaporator wettability on the heat performance of a thermosyphon by simulation and experiment, Int. J. Heat Mass Transf. 116 (2018) 675–684, https://doi.org/10.1016/j.ijheatmasstransfer.2017.09.028.

[31] Y. Kim, J. Choi, S. Kim, et al., Effects of mass transfer time relaxation parameters on condensation in a thermosyphon, J. Mech. Sci. Technol. 29 (2015) 5497–5505, https://doi.org/10.1007/s12206-015-1151-5.

[32] B. Fadhl, L.C. Wrobel, H. Jouhara, Numerical modelling of the temperature distribution in a two-phase closed thermosyphon, Appl. Therm. Eng. 60 (2013) 122–131, https://doi.org/10.1016/j.applthermaleng.2013.06.044.

[33] A.A. Alammar, R.K. Al-Dadah, S.M. Mahmoud, Numerical investigation of effect of fill ratio and inclination angle on a thermosiphon heat pipe thermal performance, Appl. Therm. Eng. 108 (2016) 1055–1065, https://doi.org/10.1016/j.applthermaleng.2016.07.163.

[34] ISO, Uncertainty of Mesurement - Part 3: Guide to the expression of uncertainty in measurement (GUM:1995), Int. Organ. Stand. Geneva ISBN (2008).

[35] C.W. Hirt, B.D. Nichols, Volume of fluid (VOF) method for the dynamics of free boundaries, J. Comput. Phys. 39 (1981) 201–225, https://doi.org/10.1016/0021-9991(81)90145-5.

[36] E. Berberović, N.P. van Hinsberg, S. Jakirlić, I.V. Roisman, C. Tropea, Drop impact onto a liquid layer of finite thickness: dynamics of the cavity evolution, Phys. Rev. E 79 (2009), 036306.

[37] J.U. Brackbill, D.B. Kothe, C. Zemach, A continuum method for modeling surface tension, J. Comput. Phys. 100 (1992) 335–354, https://doi.org/10.1016/0021-9991(92)90240-Y.

[38] A. Ferrari, I. Lunati, Direct numerical simulations of interface dynamics to link capillary pressure and total surface energy, Adv. Water Resour. 57 (2013) 19–31, https://doi.org/10.1016/j.advwatres.2013.03.005.

[39] R.W. Schrage. A Theoretical Study of Interphase Mass Transfer, Columbia University Press, 1953.

[40] G. Son, V.K. Dhir, Numerical simulation of film boiling near critical pressures with a level set method, J. Heat Transf. 120 (1998) 183–192, https://doi.org/10.1115/1.2830042.

[41] Z. Pan, J.A. Weibel, S.V. Garimella, A saturated-interface-volume phase change model for simulating flow boiling, Int. J. Heat Mass Transf. 93 (2016) 945–956, https://doi.org/10.1016/j.ijheatmasstransfer.2015.10.044.

[42] E.W. Lemmon, I.H. Bell, M.L. Huber, M.O. McLinden. NIST Standard Reference Database 23: Reference Fluid Thermodynamic and Transport Properties-REFPROP, National Institute of Standards and Technology, 2018, Version 10.0,. http://www.nist.gov/srd/nist23.cfm.

[43] B. Fadhl, L.C. Wrobel, H. Jouhara, CFD modelling of a two-phase closed thermosyphon charged with R134a and R404a, Appl. Therm. Eng. 78 (2015) 482–490, https://doi.org/10.1016/j.applthermaleng.2014.12.062.

[44] K. Hosseinzadeh, D.D. Ganji, O. Fathollah, Effect of SiO2 super-hydrophobic coating and self-rewetting fluid on two phase closed thermosyphon heat transfer characteristics: an experimental and numerical study, J. Mol. Liq. 315 (2020) 113748, https://doi.org/10.1016/j.molliq.2020.113748.

[45] Y. Kim, D.H. Shin, J.S. Kim, S.M. You, J. Lee, Effect of sintered microporous coating at the evaporator on the thermal performance of a two-phase closed thermosyphon, Int. J. Heat Mass Transf. 131 (2019) 1064–1074, https://doi.org/10.1016/j.ijheatmasstransfer.2018.11.134 (ISSN 0017–9310).